Automation in Construction 168 (2024) 105805

Contents lists available at ScienceDirect

Automation in Construction

journal homepage: www.elsevier.com/locate/autcon

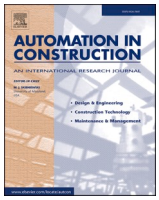

Spatio-temporal heat risk analysis in construction: Digital twin-enabled monitoring

Yoojun Kim [a], Youngjib Ham [b,*]

[a] Department of Construction Science, Texas A&M University, College Station, TX, United States
[b] Department of Civil and Environmental Engineering, Seoul National University, Seoul, South Korea

ARTICLE INFO

Keywords:
Construction safety
Heat risk
Digital twin
Microclimate simulation

ABSTRACT

To effectively mitigate heat risks, it is crucial to pinpoint areas of high vulnerability and assess the severity of heat-related threats to construction workers. This paper advances the understanding of heat risks in construction by mapping the associated risks across time and space to support informed decision-making. This paper presents a framework for heat risk monitoring, enabled by a construction site digital twin. This framework leverages geometric modeling, incorporates real-time weather data from a weather station, and utilizes computational simulations for assessing spatio-temporal heat risks. Its effectiveness was validated through a case study in Stephenville, Texas, USA, where it demonstrated superior fidelity when compared to using the conventional black-globe thermometer. Moreover, the results substantiated that incorporating the spatio-temporal variability of heat risks enhances heat risk surveillance in construction workplaces. This approach offers practical insights into imminent heat-related threats, aiming to prevent potential heat-related accidents in construction.

1. Introduction

Heat is a leading cause of weather-related fatalities, posing a serious threat to occupational health and safety [1]. Of all US industries, the construction sector is particularly susceptible to heat risks, accounting for the highest number of occupational heat-related fatalities [2]. Here, heat risk refers to the possibility that heat stress (i.e., environmental heat load on the human body) may cause harmful heat strain (i.e., physiological response to heat stress). Such harmful heat strain can lead to decreased work performance [3–5], impaired cognitive function [6–8], and an increased risk of heat-related illnesses, such as heat exhaustion and heat stroke, which are consequences of thermoregulatory failures due to extreme heat exposure [9–13]. Concerns about heat risks are intensifying in the global construction industry (e.g., Asia [14–16], Europe [17], Australia [18], and Africa [19]), with future projections indicating that climate change will worsen these issues [20].

To effectively mitigate these risks, it is imperative to understand where and to what extent heat risks threaten the health and safety of construction workers [21,22]. This knowledge leads to the development of informed heat mitigation strategies, such as implementing frequent breaks, rescheduling work activities to cooler periods, and promoting hydration. Nonetheless, measuring heat risks in outdoor environments poses challenges due to the variable nature of heat conditions, influenced by factors like shading and different surface materials [23–25]. Additionally, the dynamic nature of construction sites, where the materials and structure heights continually change with ongoing construction activities, further complicates these measurements [26]. Current methods for evaluating heat risk in outdoor construction environments typically involve mobile environmental sensors carried by workers [27] or weather stations deployed at a specific location [28–31], often fail to capture the spatial distribution of heat risks. These methods may overestimate or underestimate the risks because they do not account adequately for the spatial and temporal variations in heat exposure [32]. Consequently, this results in a gap in understanding the heat exposure faced by construction workers, posing challenges for effective safety management.

To address this knowledge gap, this study proposes a digital twin-enabled heat risk monitoring framework that facilitates spatio-temporal heat risk analysis for data-driven risk management in outdoor construction environments. As illustrated in Fig.1, this framework is designed to incorporate both visual and weather data collected from a construction site, simulate microclimates to analyze spatial heat risks, and offer actionable and timely information for risk-informed decision-making. In this context, a ‘digital twin’ refers to a geometric digital

* Corresponding author.
E-mail addresses: yoojun@tamu.edu (Y. Kim), yj.ham@snu.ac.kr (Y. Ham).

https://doi.org/10.1016/j.autcon.2024.105805
Received 21 December 2023; Received in revised form 24 September 2024; Accepted 26 September 2024
Available online 4 October 2024

replica of a construction site, synchronized with environmental conditions through an on-site weather station for continuous heat risk surveillance. Leveraging the benefits of digital modeling for site-scale heat risk analysis, this framework aims to overcome the limitations of current measurement methods and map risks across time and space, enhancing workers' heat resilience and safety.

2. Research background

2.1. Heat risk assessments in construction

Occupational safety institutions, such as the National Institute for Occupational Safety and Health (NIOSH), the Occupational Safety and Health Administration (OSHA), and the International Organization for Standardization (ISO), generally employ the wet bulb globe temperature (WBGT) to evaluate environmental heat risk [22]. WBGT is a thermo-physiological model that requires measurements of air temperature, natural wet bulb temperature, and black globe temperature [33]. NIOSH establishes Recommended Alert Limits (RALs) and Recommended Exposure Limits (RELs) based on the WBGT [22]. Similarly, ISO 7243 and OSHA provide a structured approach for assessing environmental heat stress using WBGT [33,34], while the American Conference of Governmental Industrial Hygienists (ACGIH) sets thermal limit values (TLVs) based on WBGT [35]. Guidelines from NIOSH and ISO emphasize the importance of considering both temporal and spatial factors when measuring environmental heat risks. For instance, NIOSH suggests hourly WBGT measurements during the hottest months and spatial measurements close to the work area, with separate measurements for different subareas if environmental heat varies within a single area [22]. Similarly, ISO 7243 recommends taking WBGT measurements over one hour during the hot summer months when heat stress is most likely to occur [33]. It advises addressing spatial and temporal variations by determining the necessary number of measurements and calculating an averaged WBGT value over one hour. Following these established guidelines, the initial step in managing heat risk safety is to plan how to effectively assess spatio-temporal environmental heat risk onsite.

Despite prior efforts in heat risk assessments in construction [27–31], current on-site measurement approaches have intrinsic limitations in addressing the spatio-temporal aspects of heat risk assessments. In the spatial context, previous works measure weather conditions using a mobile environmental sensor carried by a worker [27] or a weather station deployed at a single location [28–31]. Both on-site measurement approaches are limited in capturing the spatial distributions of heat risks due to challenges including logistical and cost constraints associated with multiple on-site measurements, and the need for frequent modifications to adapt to the dynamic nature of construction environments (e.g., deployment locations) [36]. These limitations can lead to inaccurate evaluations of overall heat stress levels in specific areas, as measurements are inherently affected by their specific locations [32]. Another practical aspect often overlooked is the temporal aspect, specifically the timeliness of translating weather condition measurements into environmental heat risk assessments (e.g., WBGT). Timely insights on heat risk assessment are crucial for determining robust safety management plans. However, previous works often fail to address this aspect by not clarifying how to quickly inform safety management practitioners of heat risks derived from the measured weather conditions. Such translation should be continuously accessible to practitioners for timely insights. These spatial and temporal challenges in understanding heat risk assessments in construction settings make it difficult to apply the established safety guidelines effectively to jobsites. The main objective of this study is to address this information gap by proposing a digital twin-enabled heat risk monitoring framework that overcomes spatial measurement limitations through microclimate simulation and provides actionable, data-driven insights to practitioners in a timely manner.

2.2. Digital twin applications in construction

The application of digital twins in the construction industry is still in its early stages, but has been steadily increasing in recent years [37]. Although not explicitly defined [38], the concept of a digital twin generally encompasses three key elements: a physical entity in physical space, a virtual counterpart in virtual space, and a connection between the two for data exchange [37]. In line with digitalization trends in the construction industry [39], studies have explored digital twins across different phases of construction projects, including design and engineering phase [40–42], construction phase [43,44], and operation and maintenance [45–47]. For instance, Jiang et al. [48] proposed a digital twin framework to monitor unsafe behaviors of tower crane operations. Similarly, Zheng et al. [49] introduced a digital twin framework for structural health monitoring, particularly to prevent building collapse disasters. Furthermore, Lee et al. [50] and Liang et al. [51] leveraged digital twins where a variety of dynamic site conditions are simulated as

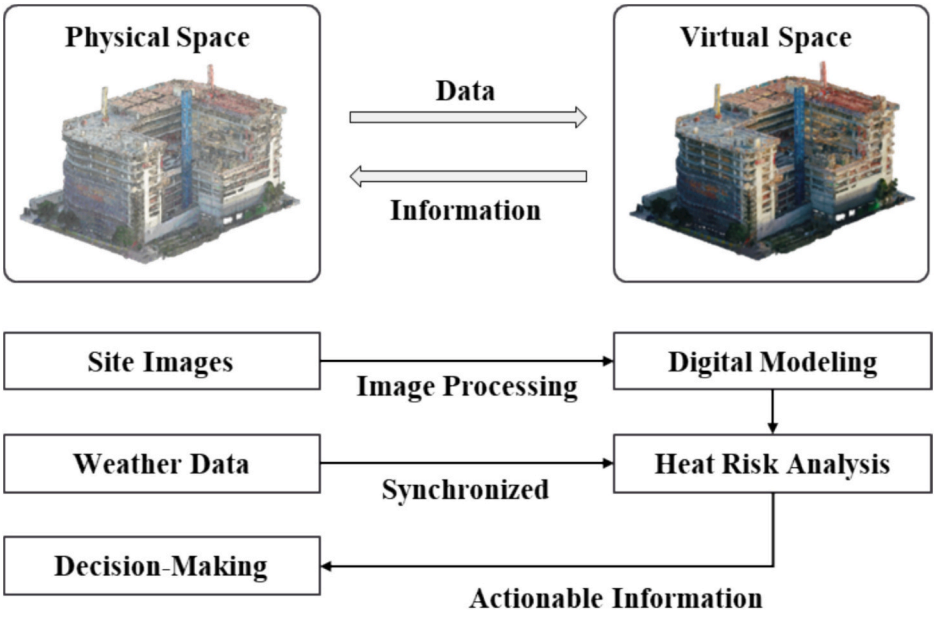

Fig. 1. Digital twin-enabled heat risk monitoring framework.

training grounds for construction robots. These studies demonstrated the potential of digital twins to enable near-real-time simulations of various scenarios offering valuable insights into how digital twins can be utilized to monitor and mitigate environmental risks. By integrating the rapid and continuous data collection of heat risk-related conditions into a virtual space, it is possible to simulate microclimates based on the collected weather conditions and geometric attributes, thereby identifying spatial heat risks in accordance with safety guidelines. This computational simulation can also evaluate potential heat mitigation scenarios, leading to more informed decision-making in construction safety management. This study explores the potential of this concept to achieve continuous spatio-temporal heat risk assessment, enabling data-driven heat risk management in construction.

3. Digital twin-enabled heat risk monitoring

3.1. Geometric data collection and processing

The geometric data is integrated into a virtual space for spatial heat risk analysis. As depicted in Fig. 2, a series of image processing techniques are employed, including UAV (Unmanned Aerial Vehicle) photogrammetry and the Canny edge detection [52]. UAV photogrammetry, a widely employed remote sensing in construction [53–58], enables the efficient collection of site images [59]. The results derived from UAV photogrammetry include both an orthophoto and geometric models of the site, such as a 3D virtual representation of the construction workplace and a digital surface model (DSM). While an orthophoto delivers a planimetric image map of the construction site [60], a DSM represents an elevation map of the site [69], offering a top-down view with spatial relationships of construction resources. As a proof of concept, the spatial resolution of DSM is set to 1 m by 1 m for data processing to integrate with other geometric datasets. Following this, exterior walls are extracted from the DSM, which has been used to identify and outline edges from construction images [61–63]. Finally, surface material information is registered into the orthophoto, which is resized to match the spatial resolution of the DSM. This procedure generates a surface material map, representing surface material types (e.g., asphalt, soil, grass) and detected wall locations.

3.2. On-site weather data synchronization via a weather station

The on-site weather data is collected and integrated into a virtual space for continuous heat risk analysis. To this end, a weather station was developed to record and transmit weather conditions through a cellular network, as shown in Fig. 3 (left). This customized weather station enables near-real-time synchronization of weather data on-site. It comprises a pyranometer (Fig. 3-①), a wind sentry anemometer (Fig. 3-②), and a temperature and relative humidity sensor (Fig. 3-③). Collectively, these sensors allow the system to capture global horizontal irradiance (GHI), air velocity (V_a), air temperature (T_a) and relative humidity (RH). The collected data is stored in two different places to ensure integrity and continuity: an internal storage device, the data logger (Fig. 3-④), and a secure digital memory card for external storage. To ensure near-real-time data transmission, the system employs a cellular module (Fig. 3-⑤) to relay the collected information to a virtual space. The graphical user interface of the data transmission is shown in Fig. 3 (right), representing the results of near-real-time transmission. The weather station is powered by a rechargeable battery (Fig. 3-⑥) with a charging regulator to ensure a consistent power supply (Fig. 3-⑦). This weather station is expected to be deployed on-site in an open area where there is no shadow interference during the daytime.

3.3. Spatio-temporal analysis of heat risk through computational simulations

Building upon the geometric and meteorological data collection outlined in Sections 3.1 and 3.2, the proposed framework conducts multi-level computational simulations to assess spatio-temporal heat risks, crucial for construction safety management. As depicted in Fig. 4, this process first generates both a shadow map and a sky view factor (SVF) map by addressing the geometric features of the construction site and the sun's position. These maps, along with a surface material map, are integrated into a physics-based microclimate simulation, resulting in a heat radiation map. This map is then utilized to compute a heat risk map, which provides valuable insights into the spatial distribution of heat risks and facilitates data-driven decision-making in line with current occupational safety guidelines. The details of each step are elaborated in the following subsections.

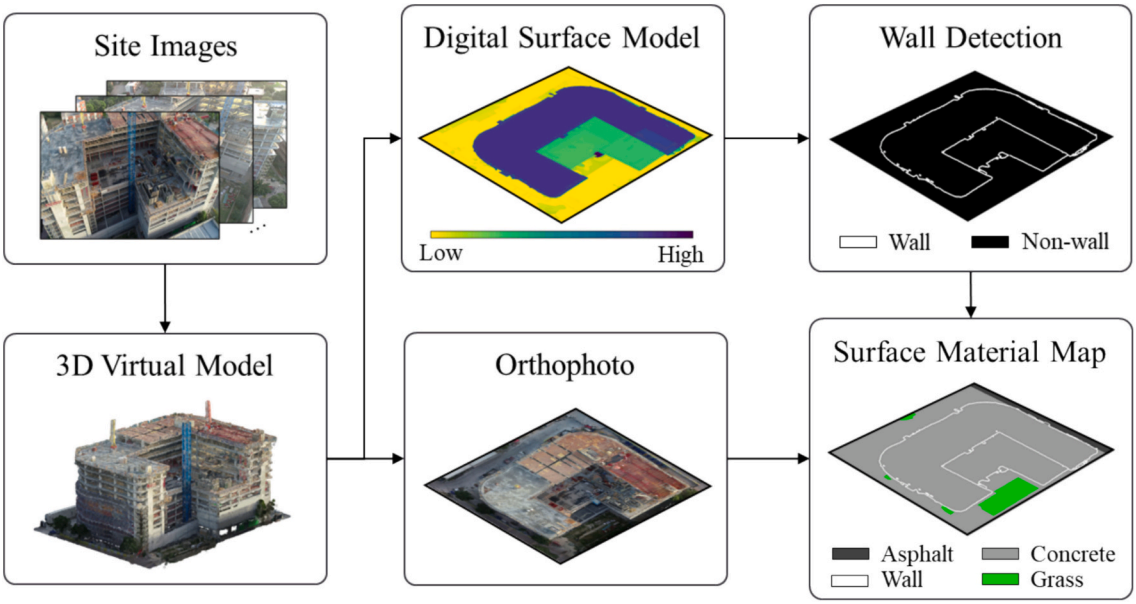

Fig. 2. Schematic workflow of geometric data processing.

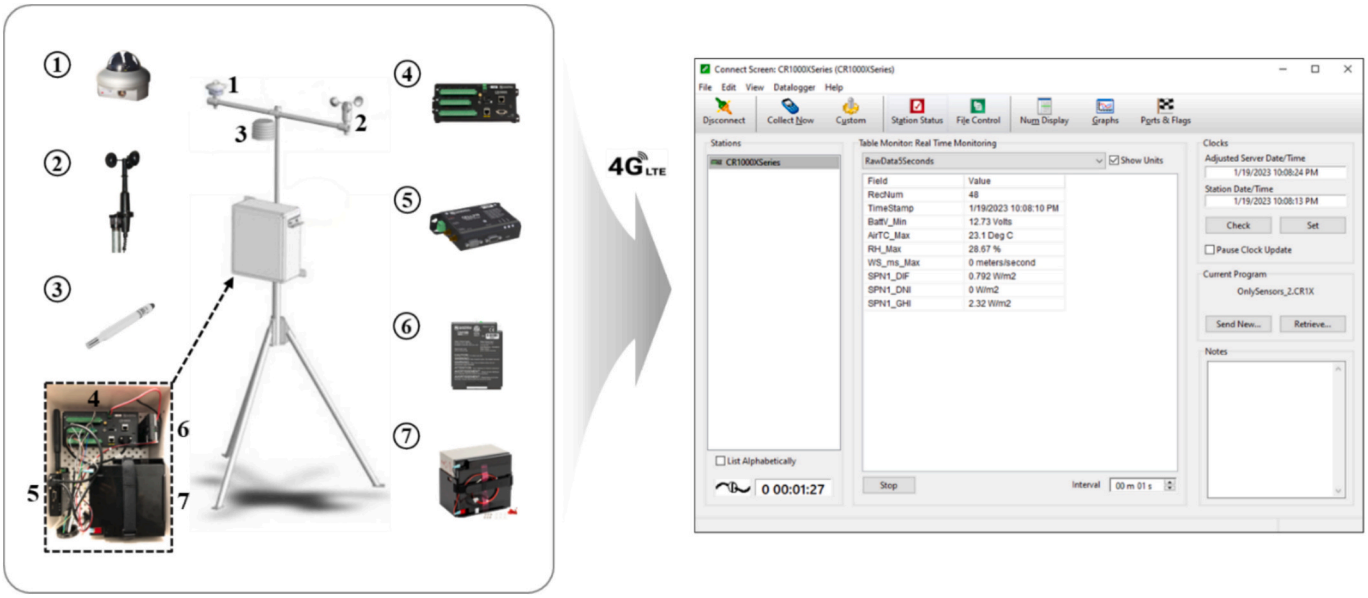

Fig. 3. Configurations of the weather station (left); example of data transmission process (right).

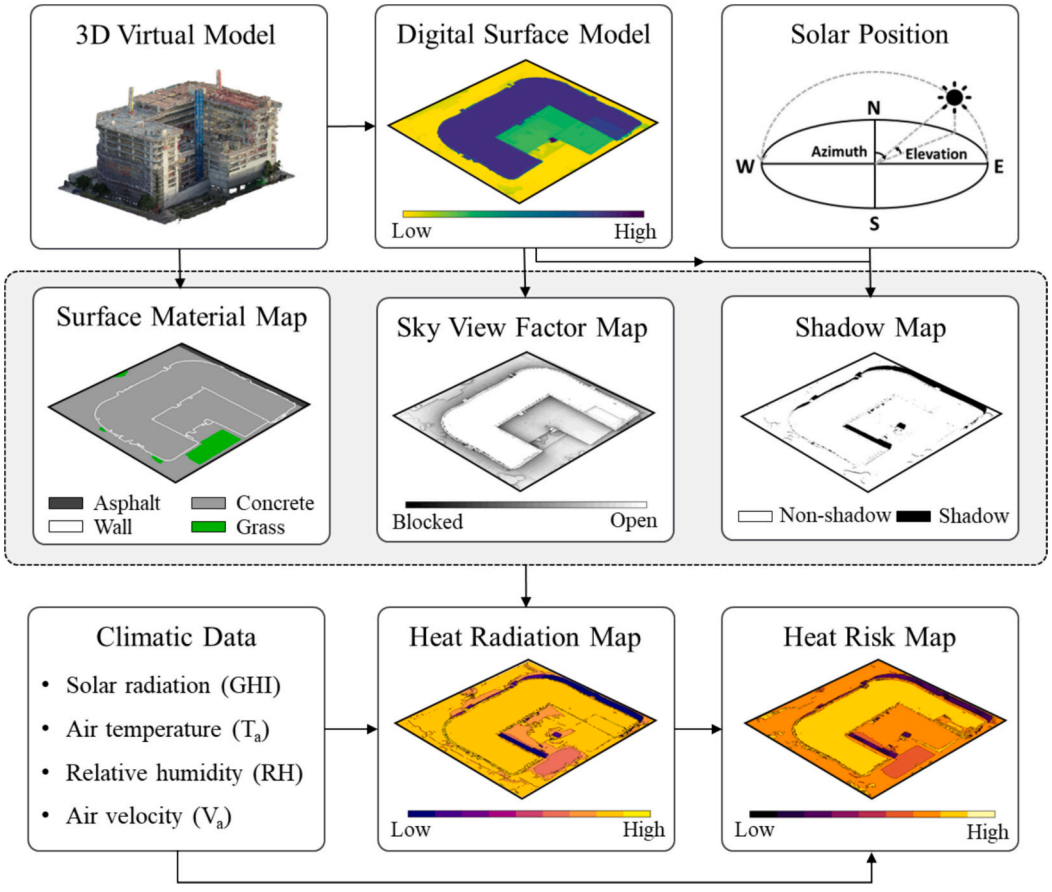

Fig. 4. Schematic workflow of spatio-temporal analysis of heat risk.

3.3.1. *Shadow map*

This study addresses the influence of shadows on heat risk distribution in outdoor construction workplaces, by generating a shadow map to ascertain whether a specific location is under shadow. This shadow map generation is a two-stage process: solar position calculation and shadow casting by considering geometric attributes of outdoor physical environments. Frist, to determine the solar position in relation to the specific site location and time, we build upon the work done by the National Renewable Energy Laboratory (NREL) [64] based on historical records of the Earth's orbit around the Sun, which has been demonstrated a high degree of precision with an uncertainty of ±0.0003° [65]. By leveraging this algorithm, the calculation of the solar angles,

including solar azimuth and solar elevation, is done for any given time and location. Subsequently, the shadows cast by surrounding built and natural environments can be estimated using trigonometric equations, as illustrated in Fig.5. To further compute the shadow patterns across construction sites, the proposed framework builds upon the DSM-based shadow casting [66], which iteratively operates at the site scale, utilizing the DSM, to provide height-related information of the construction sites. The computation begins with a 2D array of the same dimensions as the DSM, initially filled with zeros. During each iteration, the algorithm shifts the DSM by one pixel in the direction of the solar azimuth angle, simultaneously adjusting the height values based on the solar elevation angle. Thereafter, the algorithm updates the shadow volume by selecting the maximum value between the currently/previously computed 2D array. This iterative process continues until the shifted DSM either has an elevation below the original DSM in elevation or is entirely outside the original DSM region. Lastly, the shadow volume is subtracted from the original DSM, then it is converted to a Boolean image in which pixels with a negative or zero value, which are exposed to sunlight, are assigned a new value of 1, while pixels with positive values that are in shade are given a new value of 0. This Boolean image, hereby referred to as a shadow map, serves as a fundamental component for further analysis, particularly for identifying areas at high heat risk exposed to direct solar radiation in construction environments.

3.3.2. Sky view factor (SVF) map

The Sky View Factor (SVF) is crucial to characterize surface geometry to better understand radiation distributions in outdoor environments [67]. Defined as the ratio of the visible sky area from a specific point to the total hemispheric sky area [68], SVF values range between 0 and 1. A value of 0 indicates a completely blocked area, while 1 represents an open area. To generate a SVF map that conveys pixel-level SVF information, an annulus-weighted SVF computation algorithm [69] is leveraged, which operates on the principle of iteratively calculating and adding annulus weights by following the Eq. (1).

$$SVF = \sum_{i=1}^{n} S \frac{1}{\pi} sin\left(\frac{\pi}{180}\right) sin\left(\frac{\pi(2\alpha_i - 1)}{2n}\right) \frac{360}{\theta_i} \quad (1)$$

Where, n denotes the total number of shadow maps generated. S is the Boolean variable from the shadow map generated using the same shadow casting algorithm described in Section 3.3.1. α_i and θ_i are predefined elevation angles and azimuth angles in degrees, respectively. For determining these parameters, this study builds on the parameterization scheme proposed by [70], which offers the predefined set of 153 combinations of elevation angles and azimuth angles for the generation of SVF map.

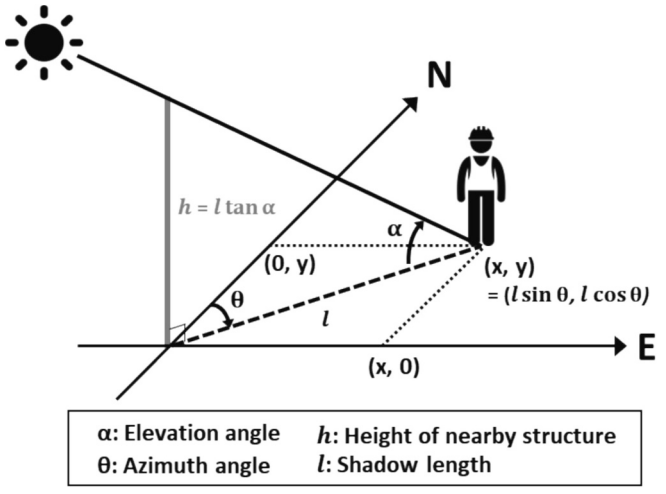

Fig. 5. Trigonometric relationship for calculating shadows based on sunlight angle.

3.3.3. Heat radiation map

Heat radiation map is generated by microclimate simulation. Microclimate simulation models [71–73] offer a promising solution to complement the limitations of on-site measurement methods. These models employ physics-based numerical simulations to emulate microclimates, taking into account geometric features, thermodynamic principles, and regional climate data [74]. This methodology overcomes the spatial constraints of on-site measurements, enabling a comprehensive heat risk analysis in complex outdoor environments. Accordingly, a growing body of literature in other disciplines, such as climatology [75,76], urban planning [77–79], and architecture [80,81], has effectively employed microclimate simulation models. This study builds on the SOlar and LongWave Environmental Irradiance Geometry (SOLWEIG) microclimate model [73] to generate a heat radiation map, which is specifically designed to analyze the spatial distribution of mean radiant temperature (T_{mrt}) in outdoor environments. T_{mrt} is a critical factor for evaluating heat radiation and inherently sensitive to both spatial and temporal variations in outdoor environments [82–84].

The SOLWEIG model comprehensively incorporates the thermodynamic principles of both built and natural environments, considering the impact of local weather conditions. It incorporates three discrete multispectral maps (i.e., surface material map, shadow map, and SVF map) and on-site weather data (i.e., T_a, RH, and GHI) collected by the weather station. The resulting heat radiation map presents the T_{mrt} distribution across construction sites. The SOLWEIG model calculates T_{mrt} using a Stephan-Boltzmann law-based equation:

$$T_{mrt} = \sqrt[4]{S_{str}/(\varepsilon_p \sigma)} + 273.15 \quad (2)$$

Here, ε_p denotes the emissivity of the human body, set at 0.97 [85], while σ represents the Stephan-Boltzmann constant (5.67×10^{-8} W/m^2·K^4). S_{str} is derived from the six-directional method, which accounts for short- and longwave radiation fluxes impacting the human body in a three-dimensional environment as per Eq. (3) [86].

$$S_{str} = \xi_k \sum_{i=1}^{6} K_i F_i + \varepsilon_p \sum_{i=1}^{6} L_i F_i \quad (3)$$

where K_i and L_i represent the shortwave and longwave radiation fluxes, respectively. The angular factors F_i, describing the geometric relationship between a person and the surrounding surfaces, are set to 0.22 for the sides and 0.06 for the above and below. The absorption coefficient for shortwave radiation, denoted as ξ_k, is set at 0.7. The calculation of K_i requires information on SVF, shadow, the sun's position, surface temperature, and GHI, while L_i calculations require information on SVF, shadow, the sun's position, surface temperature, and T_a. These parameters are computed through a series of empirical formulas documented in [87–90]. Consequently, T_{mrt} is determined once K_i and L_i are calculated, as the other variables are predefined constants.

3.3.4. Heat risk map

Mapping the spatial distribution of heat risk is crucial for identifying and managing safety risks [91]. This mapping provides actionable insights into heat risks quantified by the WBGT index or the universal thermal climate index (UTCI) [92]. The WBGT formula, as defined by the ISO 7243 standard for outdoor conditions [33], can be represented by Eq. (4):

$$WBGT = 0.7T_{nw} + 0.2T_g + 0.1T_a \quad (4)$$

Here, T_{nw} represents the natural wet bulb temperature and T_g is the globe temperature of a 0.15 m diameter black globe. To calculate T_{nw}, an empirical regression model [93] is employed, given by Eq. (5):

$$T_{nw} = T_a arctan\left[0.151977(RH + 8.313659)^{0.5}\right] + arctan(T_a + RH) - arctan(RH - 1.676331) + 0.00391838RH^{1.5} arctan(0.023101RH) - 4.686035 \quad (5)$$

Also, T_g is calculated based on the ISO 7726 standard [94] (Eq. (6)):

$$T_g{}^4 - T_{mrt}{}^4 + \frac{1.1 \times 10^8 \times V_a{}^{0.6}}{\varepsilon \times D^{0.4}} \times (T_g - T_a) = 0 \quad (6)$$

In this equation, the globe emissivity (ε) is set as 0.95 and the diameter of globe thermometer (D) is 0.15 m. T_g, the unknown value in this quartic equation, is computed based on the assumption that the solution of this quartic equation is a real number that is the closest to T_a and T_{mrt}. Following this computation, the heat radiation map is then transformed into a heat risk map, providing spatial information to identify areas with increased risk levels based on the WBGT index. Note that the WBGT index is widely recognized and employed, for example, the National Institute for Occupational Safety and Health (NIOSH) [22] and the Occupational Safety and Health Administration (OSHA) [95]. These organizations have used the WBGT index to evaluate heat risk levels, as well as to establish guidelines and recommendations for minimizing heat exposure among workers [22]. On the other hand, the UTCI is an advanced thermal index, developed using a multi-node model [96]. This index is not only applicable across all climatic zones but also capable of representing extreme thermal sensations. The UTCI has been proven as an effective estimator of thermal stress intensity in outdoor environments, affected by dynamic solar and wind conditions [97]. As a result, the UTCI map is extensively employed to assess public heat-related health risks at specific grid points for a given time [98–100].

4. Experiments and discussion

4.1. Experimental setup

The case study was conducted at an actual construction site located in Stephenville, TX (32°12′47.1"N 98°13′15.4"W) on June 18, 2023, from 6:00 to 21:00. Texas has been identified as one of the most vulnerable states to heat-related risks. In Roelofs' study [101], Texas reported the second-highest count of occupational heat fatalities from 2014 to 2016, accounting for 18 % ($n = 14$) of the total. The climate type in Texas, classified as a humid subtropical type (Cfa) by the Köppen climate classification system [102], is the common climate type of most southeastern regions in the US. Fig. 6 illustrates the geometric features of the case study site (i.e., 3D virtual model, orthophoto, DSM, and SVF). For geometric data collection and processing, 300 UAV images were collected and used for processing the 3D virtual model, DSM, and SVF, as described in Sections 3.2 and 3.3. For weather data collection, two weather stations (Stations A and B) were deployed near the site in an open area without shadows during the study period, as shown in Fig. 7. Station A is our weather station, supplemented with an additional net radiometer, while Station B includes a black-globe thermometer sensor and two net radiometers. These supplementary sensors, collecting six-directional short- and longwave radiation and black globe temperature, were used to verify the accuracy of the simulation-based method for heat risk estimation at the location described in Section 4.2. The examples of collected weather data are provided in Table 1.

Fig. 8 illustrates the weather data collected through on-site measurements in the case study site, showing the diurnal variations in T_a, RH, GHI, and V_a on the given day, with Table 1 presenting the hourly observed values. During the observation period, the T_a gradually increased from an initial value of 26 °C, reaching a peak of 35.9 °C at 16:30. Conversely, the RH exhibited a consistent decline, decreasing from 92.9 % to 37.7 % at 18:30 as shown in Fig. 8a. The sunrise occurred at 6:26, followed by sunset at 20:42, resulting in approximately 14 h of sunshine duration. The clear sky conditions were evident from the smooth shape of the GHI curve, which displayed a peak value of 1034 W/m^2 at 13:30, representing the intensity of solar radiation during that time (Fig. 8b). Furthermore, the V_a reached its maximum value of 6.1 m/s at 14:30 before following a decreasing trend (Fig. 8c). These observed weather variables were utilized in microclimate simulation and heat risk

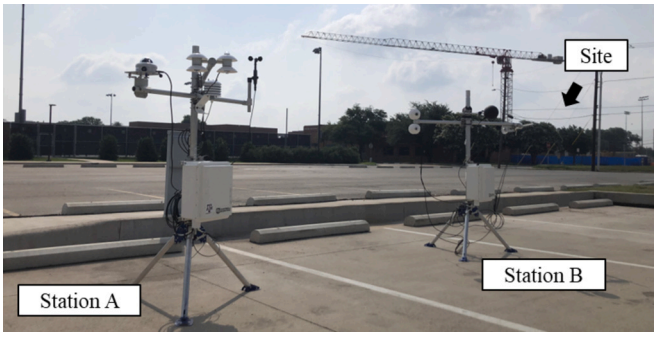

Fig. 7. Setup of the weather stations.

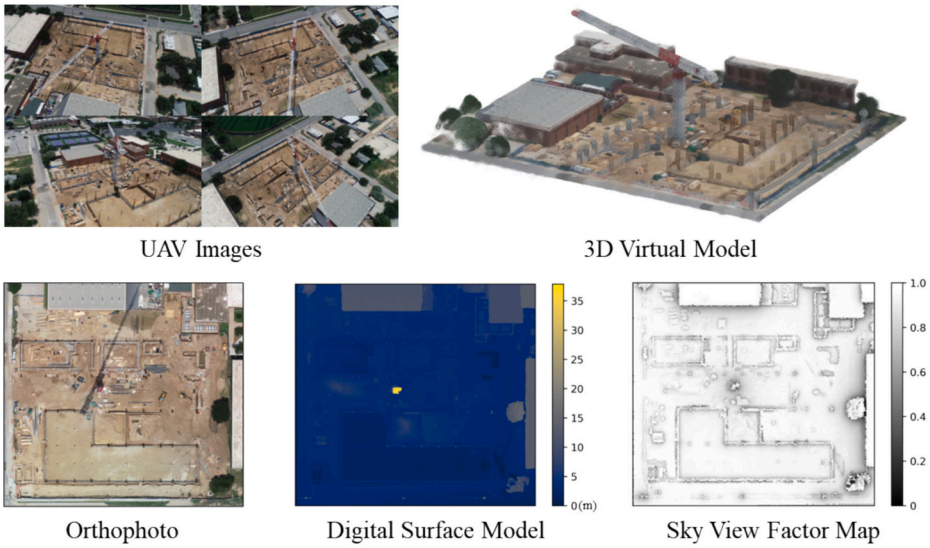

Fig. 6. Geometric features of the case study site.

Table 1
Hourly observed weather data in the case study.

Time	T_a (°C)	RH (%)	GHI (W/m^2)	V_a (m/s)
6:00	25.99	92.9	4.77	1.85
7:00	26.53	92.2	33.45	1.25
8:00	27.26	90.7	134.8	2
9:00	28.58	82.7	439.9	2.75
10:00	30.16	74.66	774	3.2
11:00	31.17	65.89	906	5.3
12:00	31.72	58.46	953	5
13:00	32.66	53.94	1029	5.3
14:00	33.63	45.76	1031	5.45
15:00	34.67	38.33	986	5.15
16:00	34.66	40.88	853	4.1
17:00	35.72	39.15	681.6	3.35
18:00	35.63	37.76	490.7	2.9
19:00	34.6	38.68	275.6	3.65
20:00	33.45	40.61	78.06	2.6
21:00	31.81	44.14	5.97	1.4

assessment to evaluate the spatio-temporal heat risks at the case study site.

4.2. Evaluation of the simulation-based method for heat risk estimation

The simulation accuracy was evaluated compared to the two measurement methods for estimating T_{mrt}, a widely used parameter for representing heat radiation. The benchmarking methods include (1) the six-directional integral radiation method [86] (hereafter the six-directional method) and (2) the black-globe thermometer method. The six-directional method is considered the most reliable technique for T_{mrt} estimation, employing three net radiometers [103]. Despite its accuracy, the high operational cost and limited mobility significantly impede its practical applications [104]. In this case study, T_{mrt} estimated by this method served as the reference to assess the accuracy of both the black-globe thermometer method and the simulation-based method. The black-globe thermometer method, grounded in the ISO 7726 standard, is widely utilized in construction-related studies [28,31,105] due to its cost-effectiveness and ease of use [106]. Nevertheless, this method often exhibits reduced precision [107] due to its inherent constraints, such as slow heat convection, especially in outdoor settings [108]. As a result, supplementary calibrations that factor in the regional weather conditions becomes necessary [109,110], which still remains overlooked in the previous works on heat analysis in jobsites. Meanwhile, the simulation-based method leverages the SOLWEIG model, detailed in Section 3.3.3. Earlier studies have validated the performance of the SOLWEIG model compared to the six-directional method when peak solar radiation is under 900 W/m^2 [111,112]. Despite these validations, there remains a dearth of understanding regarding the potential influence of inherent inaccuracies in the simulation-based method on heat risk assessments, specifically under extreme solar radiation conditions. This concern becomes especially pertinent in regions prone to high heat risks, such as Texas, where solar radiation often exceeds 1000 W/m^2 during the summer peak. In this context, this study evaluates the accuracy of the simulation-based method for heat risk estimation under extreme solar radiation conditions. In our microclimate simulation, we adjust the albedo and emissivity of the ground surface to 0.15 and 0.95 respectively, referring to [113]. The simulation results are compared to the T_{mrt} estimated by the black-globe thermometer method. The performance of these two methods is compared using two statistical measures: the root mean square error (RMSE) and the coefficient of determination (R^2). The RMSE represents the total error in the linear model fit of the methods, while R^2 indicates the proportion of the total variance. Therefore, a lower RMSE (closer to 0) and a higher R^2 (closer to 1) indicate superior performance, more closely aligning with the reference data obtained from the six-directional method.

Fig. 9a and b display the results of three methods used to estimate T_{mrt} at half-hour intervals, from 6:00 to 21:00, during the case study period. When comparing the results derived from the black-globe thermometer method and the simulation-based method, the latter demonstrates a superior performance, featuring a RMSE of 4.21 °C and a R^2 of 0.93. This method, however, exhibits a slight tendency to overestimate T_{mrt} after 14:00. Conversely, the black-globe thermometer method reveals substantial discrepancies, with an RMSE of 11.80 °C and an R^2 of 0.44. Errors appear to increase in severity when T_{mrt} is higher, peaking at a maximum difference of 20.86 °C at 10:00. Fig. 9c presents the resultant heat risks, as assessed by the UTCI. The heat risks assessed by the T_{mrt} from the six-directional and simulation-based methods correspond closely in terms of their heat stress classification levels (i.e., moderate, strong, and very strong heat stress, refer to Table 2). However, the heat risks assessed by the T_{mrt} from the black-globe thermometer method differ significantly in their stress levels between 8:30 and 15:00. This discrepancy highlights the errors associated with the black-globe thermometer method and how these errors can distort the overall perception of heat risks in our case study. Consequently, this finding underscores the need for calibration of the black-globe thermometer method to incorporate regional weather conditions in jobsites, which has been unaddressed in prior research.

We further investigated the potential for calibrating the albedo and emissivity values of ground surfaces when using a simulation-based method. In our case study, we empirically adjusted the albedo and emissivity to 0.33 and 0.81, respectively. Fig. 10 depicts the improvements achieved through this calibration. For upward shortwave radiation (K_{up}), the RMSE dropped significantly from 120.36 to 5.50, while R^2 improved substantially from 0.06 to 1.0, compared to the observed K_{up} (Fig. 10a). For upward longwave radiation (L_{up}), the RMSE declined from 89.64 to 35.95, and the R^2 rose from −4.57 to 0.10, relative to the observed L_{up} (Fig. 10b). Consequently, the RMSE of T_{mrt} estimation reduced from 4.21 to 4.12 (Fig. 10c). This adjustment emphasizes the significance of selecting appropriate albedo and emissivity values for ground surface materials. However, the extensive variation in material properties typically found on-site presents an underlying challenge to

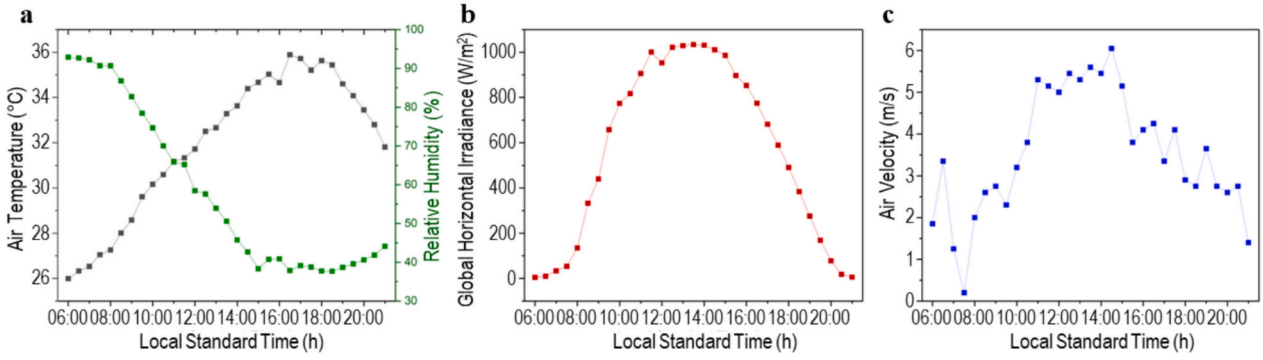

Fig. 8. Observed weather trends in the case study: (a) T_a and RH, (b) GHI, and (c) V_a.

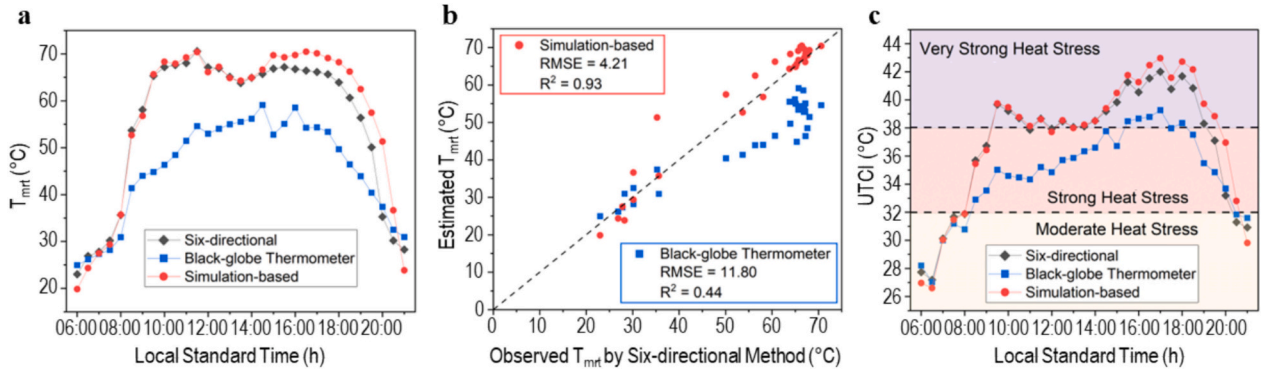

Fig. 9. (a) T_{mrt} estimation across three methods, (b) T_{mrt} estimations by simulation-based and black-globe thermometer methods compared to the reference data, (c) heat risk assessments derived from three T_{mrt} estimation methods.

Table 2
Classes of the heat risk levels for the Heat Index, WBGT index, and UTCI.

Heat Index [114]		WBGT index [22]		UTCI [115]	
Class	Index (°C)	Class	Index (°C)	Class	Index (°C)
None	below 27	None	below 25.6	No thermal stress	9 to 26
Caution	27 to 32	Category 1	25.6 to 27.8	Moderate heat stress	26 to 32
Extreme caution	32 to 41	Category 2	27.8 to 29.5	Strong heat stress	32 to 38
Danger	41 to 54	Category 3	29.5 to 31.1	Very strong heat stress	38 to 46
Extreme danger	above 54	Category 4	31.1 to 32.2	Extreme heat stress	above 46
–	–	Category 5	above 32.2	–	–

this task. In Section 4.4, we further discuss a potential solution to this issue, focusing particularly on surface temperature estimation, which influences longwave radiation trends.

4.3. Spatio-temporal heat risk assessments via the proposed framework

By leveraging computational simulations, the proposed framework advances spatio-temporal heat risk assessments. Fig. 11 provides a visual depiction of the resultant spatio-temporal distribution of T_{mrt} by the proposed framework. The estimated T_{mrt} demonstrates substantial spatio-temporal variability, with values between 22 °C and 82 °C. This variability is influenced by weather factors, including GHI, T_a, and RH. The impact of geometrical features, such as surface materials and shading from proximal structures, further contributes to these spatio-temporal complexities. For instance, during our case study, we observed a T_{mrt} differential of 43.28 °C at 16:30, a result of heterogeneity in surface materials and shading patterns. From these findings, it can be inferred that larger and more architecturally complex construction sites, characterized by a variety of surface materials and structures (including adjacent high-rise buildings), could exhibit even greater variability. This underscores the significance of performing heat radiation assessments to gain a comprehensive spatio-temporal understanding of potential heat risks on construction sites.

Next, we conducted a comparative study exploring spatial variations in heat risks based on three heat indices: the Heat Index, the WBGT index, and the UTCI. To enable effective comparisons, we classified the levels of heat risks for each index, as detailed in Table 2. The Heat Index, derived from T_a and RH, is unable to capture spatial variations as it excludes heat radiation variations from its calculation, as shown in Fig. 12a. On the other hand, the WBGT index and UTCI represent the spatio-temporal trends of minimum, mean, and maximum values, aligning with the classified heat risk levels in Fig. 12b and c. Fig. 12d provides an hourly assessment of the variances in heat risks as evaluated by these three heat indices. Notably, even within identical construction sites and similar weather conditions, heat risk levels can vary significantly based on the type of heat indices applied and the areas of focus. Overlooking such variations could lead to either underestimation or overestimation of heat risks, depending on measurement locations. Such omissions may obscure crucial insights into the diverse exposure levels of construction workers, which could vary based on their work locations and durations. The proposed approach has the potential to offer insights that can advance the understanding of heat stress levels, which lead to the development of effective heat mitigation strategies.

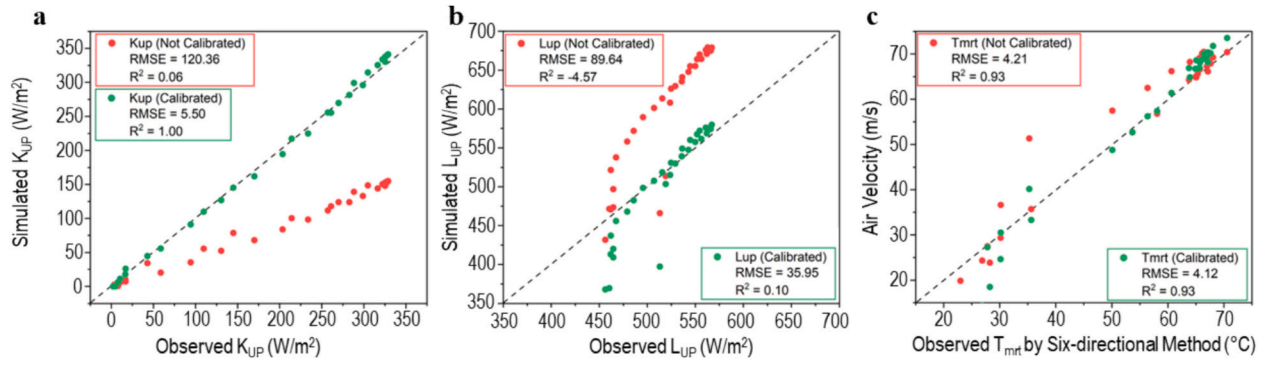

Fig. 10. Pre and post-calibration (a) upward shortwave radiation of simulation-based method, (b) upward longwave radiation of simulation-based method, (c) T_{mrt} estimation comparison for simulation-based method.

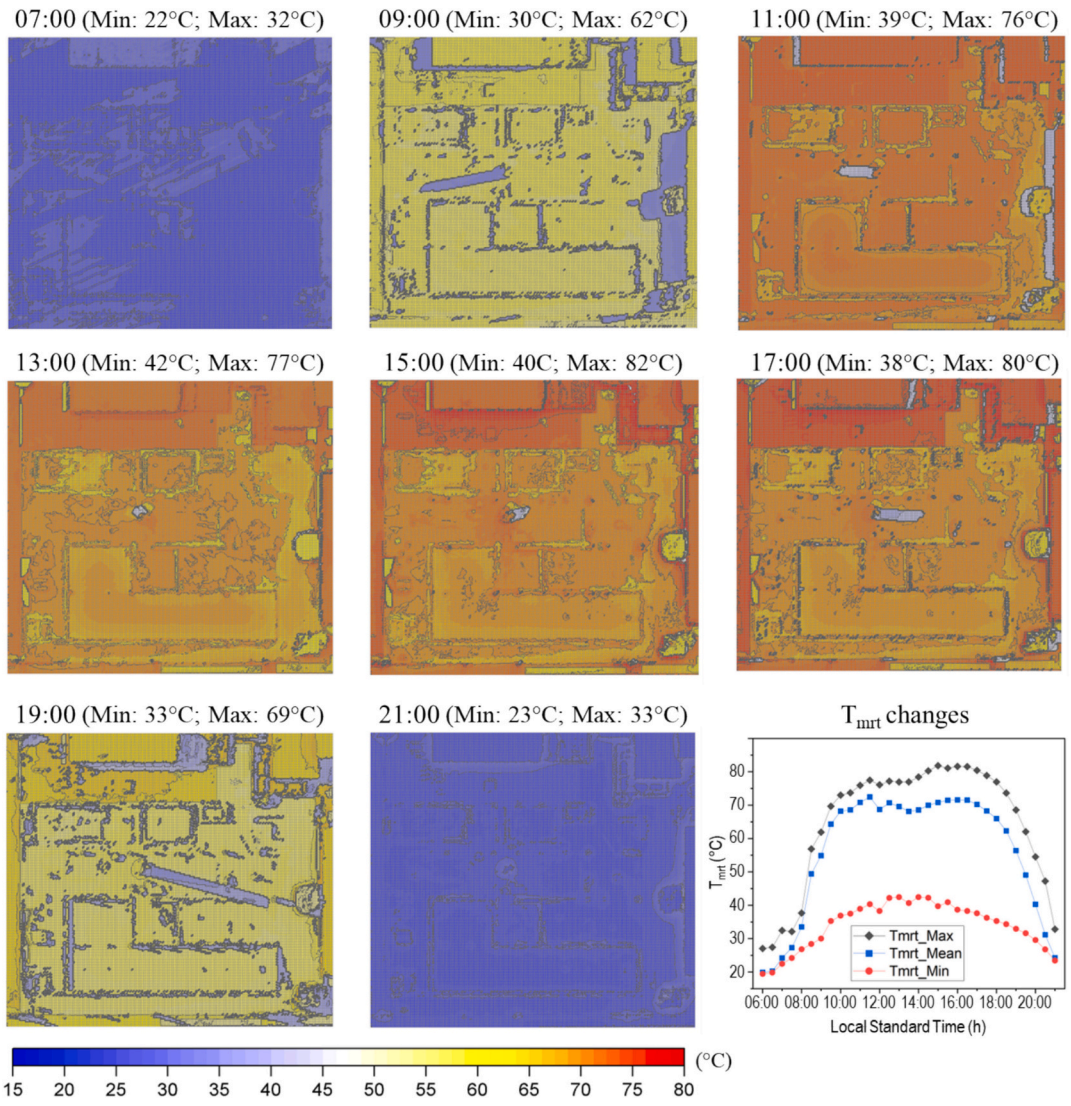

Fig. 11. Spatio-temporal variations of T_{mrt} in the case study.

4.4. Integrating infrared thermography for enhanced surface temperature estimations

In Section 4.2, the variations in onsite material properties were highlighted as a challenge in achieving accurate surface temperature estimations. Recognizing this, an approach incorporating infrared thermography was employed to evaluate the accuracy of simulation-based estimations of surface temperature and explore alternative methods. Utilizing the thermal camera, hourly surface temperatures of construction materials including asphalt, plywood, and soil were recorded, as shown in Fig. 13a, b, and c. The results revealed that plywood recorded a peak temperature of 58.9 °C at 14:00 (Fig. 13d). In comparison, soil and asphalt showed temperatures of 55.7 °C and 51.7 °C, respectively. These findings indicate that, under the given climate conditions, plywood retains more heat than both soil and asphalt. Furthermore, upon comparing the observed temperatures with the simulation results for asphalt and soil (Fig. 13e and Fig. 13f), the simulation results consistently yielded overestimated values, with the largest deviations recorded as 23.6 °C for asphalt at 14:00 and 16.3 °C for soil at 10:00.

Understanding the surface temperatures enhances the insights into spatial heat distribution in outdoor settings [116–118]. However, simulating these thermal distributions poses underlying challenges. First, as highlighted in Fig. 13, simulating surface temperatures using predetermined factors and weather variables, such as T_a and RH, is complicated given the intricate and diverse nature of surface materials. This challenge becomes even more pronounced in areas with intense sunlight radiation, leading to unpredictable surface temperature patterns [119]. Second, manually registering surface materials to generate a surface material map is time-consuming and labor-intensive. This challenge becomes particularly problematic in dynamic construction settings, where surface materials continuously change, and heat risk assessments need to be conducted promptly.

To address these challenges, we conducted extensive research into the potential of incorporating UAV infrared thermography into a digital twin framework as a proof-of-concept. This has been studied in structural health monitoring due to its rapid data gathering [120–122], and has demonstrated its efficiency in mapping surface temperatures in urban settings [123]. In our case study, we utilized a FLIR Vue Pro R thermal camera to capture surface temperatures at five distinct intervals, as shown in Fig. 14. A notable finding was the consistently elevated temperatures on roofs of the surrounding buildings, highlighting a potential area for improvement in the SOLWEIG model that takes account of the associated thermal properties. Furthermore, our findings indicated that soil surfaces consistently show higher temperatures than concrete, aligning with the findings from Fig. 13a. A

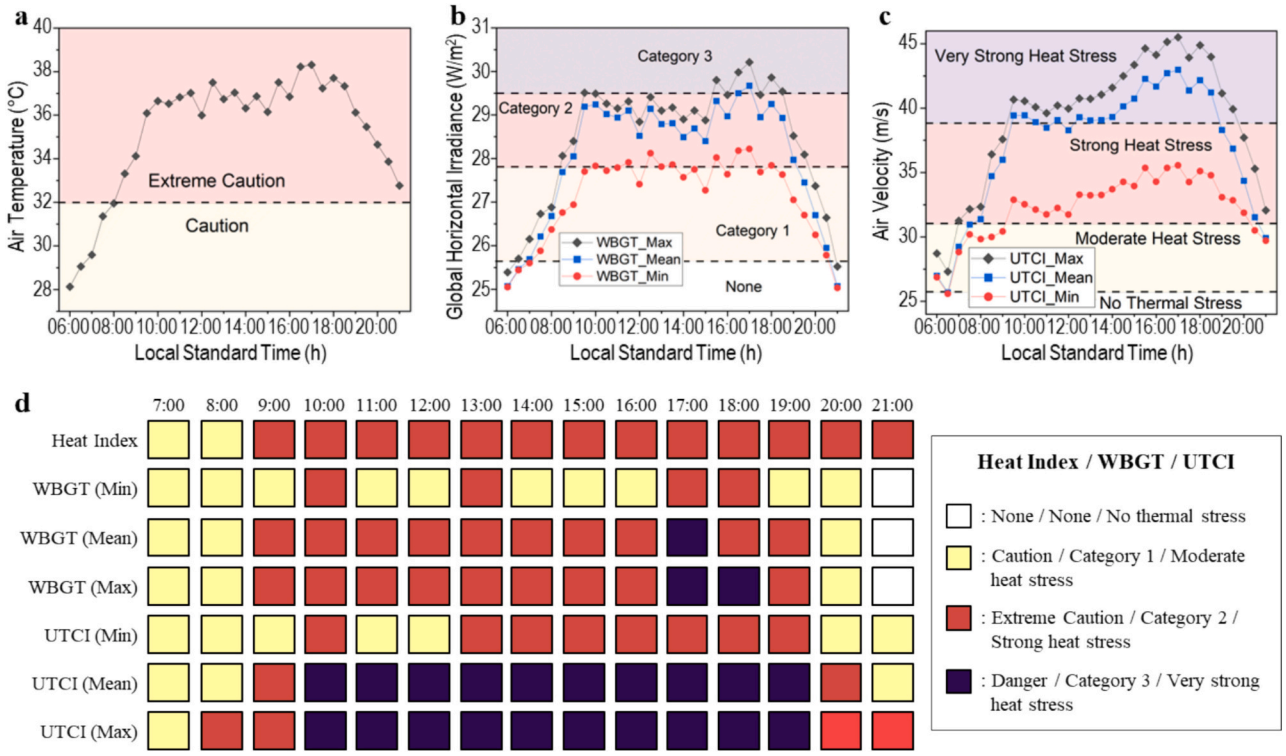

Fig. 12. Spatial variations in heat risk assessments: hourly distributions of heat risks assessed by (a) the Heat Index, (b) WBGT index, and (c) UTCI, with (d) hourly variations in heat risk levels assessed by the three heat indices.

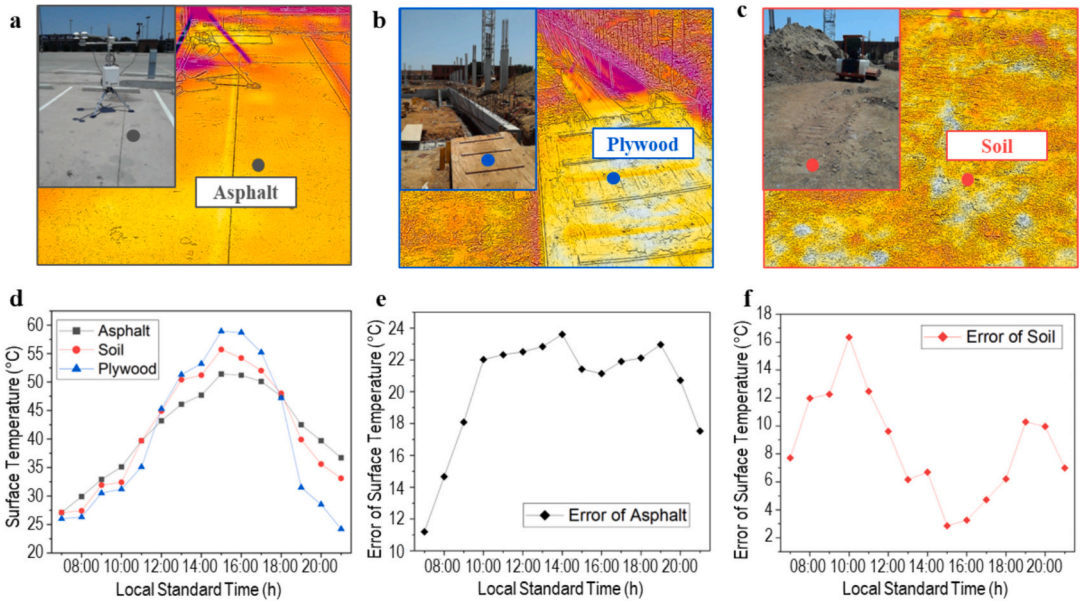

Fig. 13. Surface temperature measurements of (a) asphalt, (b) plywood, (c) soil, along with (d) observed data for different materials, (e) deviations in asphalt surface temperatures, and (f) deviations in soil surface temperatures.

significant surface temperature difference of up to 53 °C was observed between the highest and lowest surface temperatures recorded during the fourth interval. While UAV infrared thermography exhibits promise in capturing surface temperatures in construction environments, it does have certain limitations that require addressing for future implementation within the digital twin framework, especially concerning data processing efficiency. This limitation largely stems from the computational demands of collecting and processing thermal images on a site-wide scale within reduced timeframes.

4.5. *Practical implications and limitations*

The proposed framework aims to enhance heat resilience and safety for construction workers in outdoor environments. By utilizing geometric image processing and computational simulations, the framework provides near-real-time heat risk information at construction sites, offering actionable insights and establishing a foundation for data-driven heat mitigation solutions. Notably, except for the vision-based site geometric modeling, all processes in the framework are fully automated.

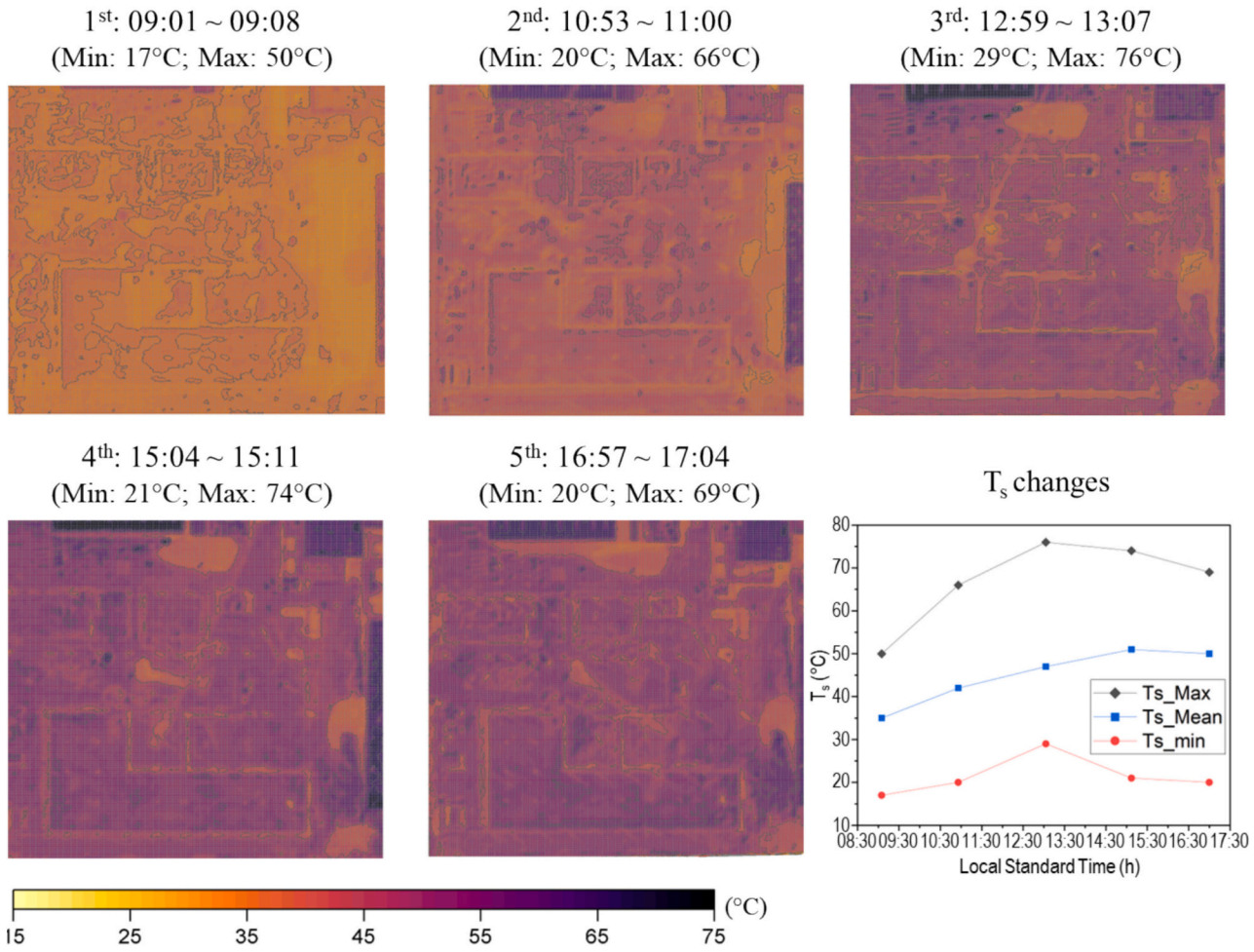

Fig. 14. Spatio-temporal surface temperature variations using infrared thermography.

This study contributes to two aspects of literature and industry. Firstly, the framework offers essential and timely insights for managing heat risks at the site level using established occupational heat risk metrics like the WBGT index and the UTCI. It addresses limitations of on-site weather measurements by considering the spatio-temporal contexts of heat risks, as recommended by NIOSH [22] and ISO [33]. Additionally, it provides near-real-time heat risk information to inform heat mitigation strategies, including managing heat exposure of construction workers using RELs/RALs [22] and TLVs [35]. Secondly, the framework provides heat risk maps in a timely manner, which are crucial for safety management. As evidenced in [124–126], risk maps are effective safety communication tools that effectively identify high-risk zones and facilitate proactive safety decisions. Beyond visualization, this data layer can enhance the granularity of safety management in future studies. For example, a prior study [127] used heat radiation maps with GPS trajectory data to estimate outdoor heat exposure. Building on these insights, the heat risk map in this framework can estimate the outdoor heat exposure of construction workers if their locations are tracked. These approaches can be connected to established safety standards, facilitating the use of individual exposure data for improved assessments of heat-related risks.

Despite the insights this study offers, there are still open research challenges and limitations for improving the proposed framework. First, although the SOLWEIG model has been widely utilized and validated in various fields for its reliability [88–90], careful data interpretation is required as undetectable and random errors are inevitable, as with other numerical simulation models [128]. For example, our study highlights the need to improve the thermophysical attributes of construction materials, which results in deviations in surface temperature estimation and influences longwave radiation trends. As a proof-of-concept, we explore an alternative solution using UAV infrared thermography to minimize surface temperature estimation errors in Section 4.4. However, the computational demands of collecting and processing thermal images on a site-wide scale inhibit its practical implementation on-site. Second, while geometric data collection and processing are geometry-free approaches that can address various geometrical elements with differing shapes, the update of geometric attributes is directly dependent on the update and processing of UAV images. Since the geometric virtual model is not synchronized in the proposed framework, geometric updates between image updates may not be reflected in the simulation results. For example, if UAV images are updated daily, the geometric features of structures erected on that day or moving objects (e.g., excavators, tower crane booms) are not addressed in the proposed framework. In this context, integrating other reality capture technologies (e.g., laser scanners) [129] or plans [130] can be considered to minimize the update time for geometric attributes, which is beyond the scope of this study.

5. Conclusion

Heat risk is a pressing safety concern in the construction industry, requiring a comprehensive understanding to effectively safeguard workers' health and safety. Current analysis methods lack a focus on spatial and temporal aspects, hindering effective heat risk assessment and management in outdoor environments. To address this gap, this paper proposes a framework based on the concept of a digital twin. The proposed framework was evaluated through a case study in

Stephenville, Texas, USA, and it showed superior fidelity compared to the conventional approach based on black-globe thermometer. By leveraging near-real-time heat risk maps and simulations, stakeholders can visualize high-risk areas in terms of heat-related hazards and deploy targeted interventions, enhancing the protection of construction workers against increasing heat-related challenges. Future research could further enhance this framework by integrating biometric sensors for real-time monitoring of workers' physiological responses to outdoor heat environments. These advancements could lead to more individualized and robust heat risk assessments, contributing to improved construction safety measures.

CRediT authorship contribution statement

Yoojun Kim: Writing – original draft, Visualization, Validation, Methodology, Investigation. **Youngjib Ham:** Writing – review & editing, Supervision, Resources, Project administration, Methodology, Investigation, Conceptualization.

Declaration of competing interest

The authors declare that they have no known competing financial interests or personal relationships that could have appeared to influence the work reported in this paper.

Data availability

Some or all data, models, or code that support the findings of this study are available from the corresponding author upon reasonable request.

Acknowledgement

This material is in part based upon work supported by the National Science Foundation (NSF) under Award #2126045. Any opinions, findings, and conclusions or recommendations expressed in this material are those of the authors and do not necessarily reflect the views of the NSF.

References

[1] FACT SHEET, Biden Administration Mobilizes to Protect Workers and Communities from Extreme Heat, The White House, 2021. https://www.whitehouse.gov/briefing-room/statements-releases/2021/09/20/fact-sheet-biden-administration-mobilizes-to-protect-workers-and-communities-from-extreme-heat/ (accessed May 22, 2023).
[2] X.S. Dong, G.H. West, A. Holloway-Beth, X. Wang, R.K. Sokas, Heat-related deaths among construction workers in the United States, Am. J. Ind. Med. 62 (2019) 1047–1057, https://doi.org/10.1002/ajim.23024.
[3] T. Kjellstrom, I. Holmer, B. Lemke, Workplace heat stress, health and productivity – an increasing challenge for low and middle-income countries during climate change, Glob. Health Action 2 (2009) 2047, https://doi.org/10.3402/gha.v2i0.2047.
[4] W. Szewczyk, I. Mongelli, J.-C. Ciscar, Heat stress, labour productivity and adaptation in Europe—a regional and occupational analysis, Environ. Res. Lett. 16 (2021) 105002, https://doi.org/10.1088/1748-9326/ac24cf.
[5] L.A. Parsons, D. Shindell, M. Tigchelaar, Y. Zhang, J.T. Spector, Increased labor losses and decreased adaptation potential in a warmer world, Nat. Commun. 12 (2021) 7286, https://doi.org/10.1038/s41467-021-27328-y.
[6] T.S. Abdelhamid, J.G. Everett, Physiological demands during construction work, J. Constr. Eng. Manag. 128 (2002) 427–437, https://doi.org/10.1061/(ASCE)0733-9364(2002)128:5(427).
[7] C.M. Nizam, A.R. Ismail, E.H. Sukadrin, N.K. Mokhtar, A. Abdullah, N. Jusoh, N. Husshin, A short review on heat stress and heat strain in construction industry: the effect on worker performance, associated health effect, it's measurement and control mechanism, in: M.H.A. Hassan, Z. Ahmad Manap, M.Z. Baharom, N. H. Johari, U.K. Jamaludin, M.H. Jalil, I. Mat Sahat, M.N. Omar (Eds.), Human-Centered Technology for a Better Tomorrow, Springer Singapore, Singapore, 2022, pp. 559–566, https://doi.org/10.1007/978-981-16-4115-2_45.
[8] P.A. Hancock, I. Vasmatzidis, Effects of heat stress on cognitive performance: the current state of knowledge, Int. J. Hyperth. 19 (2003) 355–372, https://doi.org/10.1080/0265673021000054630.
[9] J.K. Vanos, J.W. Baldwin, O. Jay, K.L. Ebi, Simplicity lacks robustness when projecting heat-health outcomes in a changing climate, Nat. Commun. 11 (2020) 6079, https://doi.org/10.1038/s41467-020-19994-1.
[10] T. Kakamu, S. Endo, T. Hidaka, Y. Masuishi, H. Kasuga, T. Fukushima, Heat-related illness risk and associated personal and environmental factors of construction workers during work in summer, Sci. Rep. 11 (2021) 1119, https://doi.org/10.1038/s41598-020-79876-w.
[11] R. Takegawa, J. Kanda, A. Yaguchi, S. Yokobori, K. Hayashida, A prehospital risk assessment tool predicts clinical outcomes in hospitalized patients with heat-related illness: a Japanese nationwide prospective observational study, Sci. Rep. 13 (2023) 1189, https://doi.org/10.1038/s41598-023-28498-z.
[12] L.L. Jackson, H.R. Rosenberg, Preventing heat-related illness among agricultural workers, J. Agromedicine 15 (2010) 200–215, https://doi.org/10.1080/1059924X.2010.487021.
[13] B.M. Varghese, A. Hansen, P. Bi, D. Pisaniello, Are workers at risk of occupational injuries due to heat exposure? A comprehensive literature review, Saf. Sci. 110 (2018) 380–392, https://doi.org/10.1016/j.ssci.2018.04.027.
[14] S. Yasmeen, H. Liu, Y. Wu, B. Li, Physiological responses of acclimatized construction workers during different work patterns in a hot and humid subtropical area of China, J. Build. Eng. 30 (2020) 101281, https://doi.org/10.1016/j.jobe.2020.101281.
[15] R. Inaba, S.M. Mirbod, Comparison of subjective symptoms and hot prevention measures in summer between traffic control workers and construction Workers in Japan, Ind. Health 45 (2007) 91–99, https://doi.org/10.2486/indhealth.45.91.
[16] J. Chinnadurai, V. Venugopal, K. P, P. R, Influence of occupational heat stress on labour productivity – a case study from Chennai, India, Int. J. Product. Perform. Manag. 65 (2016) 245–255, https://doi.org/10.1108/IJPPM-08-2014-0121.
[17] J. Pérez-Alonso, Á.J. Callejón-Ferre, Á. Carreño-Ortega, J. Sánchez-Hermosilla, Approach to the evaluation of the thermal work environment in the greenhouse-construction industry of SE Spain, Build. Environ. 46 (2011) 1725–1734, https://doi.org/10.1016/j.buildenv.2011.02.014.
[18] J. Xiang, P. Bi, D. Pisaniello, A. Hansen, T. Sullivan, Association between high temperature and work-related injuries in Adelaide, South Australia, 2001–2010, Occup. Environ. Med. 71 (2014) 246–252, https://doi.org/10.1136/oemed-2013-101584.
[19] K. Seema, C. Aigbavboa, Assessment of heat stress impacts on construction workers: A south African exploratory study, in: R.S. Goonetilleke, W. Karwowski (Eds.), Advances in Physical Ergonomics and Human Factors, Springer International Publishing, Cham, 2018, pp. 455–465, https://doi.org/10.1007/978-3-319-60825-9_48.
[20] A.M. Al Refaie, A.M. Alashwal, Z. Abdul-Samad, H. Salleh, Weather and labor productivity in construction: a literature review and taxonomy of studies, IJPPM 70 (2020) 941–957, https://doi.org/10.1108/IJPPM-12-2019-0577.
[21] S. Rowlinson, A. YunyanJia, B. Li, C. ChuanjingJu, Management of climatic heat stress risk in construction: a review of practices, methodologies, and future research, Accid. Anal. Prev. 66 (2014) 187–198, https://doi.org/10.1016/j.aap.2013.08.011.
[22] B. Jacklitsch, W.J. Williams, K. Musolin, A. Coca, J.-H. Kim, N. Turner, Occupational Exposure to Heat and Hot Environments, Department of Health and Human Services, Centers for Disease Control and Prevention, 2016. https://stacks.cdc.gov/view/cdc/37911.
[23] H. Guo, D. Aviv, M. Loyola, E. Teitelbaum, N. Houchois, F. Meggers, On the understanding of the mean radiant temperature within both the indoor and outdoor environment, a critical review, Renew. Sust. Energ. Rev. 117 (2020) 109207, https://doi.org/10.1016/j.rser.2019.06.014.
[24] B. Jänicke, F. Meier, F. Lindberg, S. Schubert, D. Scherer, Towards city-wide, building-resolving analysis of mean radiant temperature, Urban Clim. 15 (2016) 83–98, https://doi.org/10.1016/j.uclim.2015.11.003.
[25] D. Aviv, H. Guo, A. Middel, F. Meggers, Evaluating radiant heat in an outdoor urban environment: resolving spatial and temporal variations with two sensing platforms and data-driven simulation, Urban Clim. 35 (2021) 100745, https://doi.org/10.1016/j.uclim.2020.100745.
[26] Y. Kim, Y. Ham, Heat stress monitoring in construction for risk-informed decision-making, in: Construction Research Congress 2024, American Society of Civil Engineers, Des Moines, Iowa, 2024, pp. 70–78, https://doi.org/10.1061/9780784485262.008.
[27] I. Szer, T. Lipecki, J. Szer, K. Czarnocki, Using meteorological data to estimate heat stress of construction workers on scaffolds for improved safety standards, Autom. Constr. 134 (2022) 104079, https://doi.org/10.1016/j.autcon.2021.104079.
[28] D.P. Wong, J.W. Chung, A.P. Chan, F.K. Wong, W. Yi, Comparing the physiological and perceptual responses of construction workers (bar benders and bar fixers) in a hot environment, Appl. Ergon. 45 (2014) 1705–1711, https://doi.org/10.1016/j.apergo.2014.06.002.
[29] W. Yi, A.P.C. Chan, X. Wang, J. Wang, Development of an early-warning system for site work in hot and humid environments: a case study, Autom. Constr. 62 (2016) 101–113, https://doi.org/10.1016/j.autcon.2015.11.003.
[30] A.P.C. Chan, W. Yi, D.W.M. Chan, D.P. Wong, Using the thermal work limit as an environmental determinant of heat stress for construction workers, J. Manag. Eng. 29 (2013) 414–423, https://doi.org/10.1061/(ASCE)ME.1943-5479.0000162.
[31] A.P.C. Chan, M.C.H. Yam, J.W.Y. Chung, W. Yi, Developing a heat stress model for construction workers, J. Facil. Manag. 10 (2012) 59–74, https://doi.org/10.1108/14725961211200405.
[32] Y. Kim, Y. Ham, Revealing the impact of heat radiation on construction: a microclimate simulation using meteorological data and geometric modeling,

J. Constr. Eng. Manag. 150 (2024) 04024016, https://doi.org/10.1061/JCEMD4.COENG-14023.
[33] International Organization for Standardization (ISO) (Ed.), ISO 7243:2017 Ergonomics of the thermal environment Assessment of heat stress using the WBGT (wet bulb globe temperature) index, 3rd ed., International Organization for Standardization (ISO), Geneva, Switzerland, 2017 https://doi.org/10.31030/2655582.
[34] Occupational Safety and Health Administration (OSHA), OSHA Technical Manual (OTM) Section III: Chapter 4. https://www.osha.gov/otm/section-3-health-hazards/chapter-4#wbgt, 2017 (accessed June 13, 2024).
[35] American Conference of Governmental Industrial Hygienists (ACGIH), Threshold Limit Values (TLVs) and Biological Exposure Indices (BEIs) 2021, American Conference of Governmental Industrial Hygienists, Cincinnati, OH, 2021. ISBN: 978-1607261452.
[36] Y. Kim, Y. Ham, Digital twin-based heat stress monitoring system in construction, in: Computing in Civil Engineering 2023, American Society of Civil Engineers, Corvallis, Oregon, 2024, pp. 664–671, https://doi.org/10.1061/9780784485248.080.
[37] V.V. Tuhaise, J.H.M. Tah, F.H. Abanda, Technologies for digital twin applications in construction, Autom. Constr. 152 (2023) 104931, https://doi.org/10.1016/j.autcon.2023.104931.
[38] D.-G.J. Opoku, S. Perera, R. Osei-Kyei, M. Rashidi, Digital twin application in the construction industry: a literature review, J. Build. Eng. 40 (2021) 102726, https://doi.org/10.1016/j.jobe.2021.102726.
[39] S.K. Baduge, S. Thilakarathna, J.S. Perera, M. Arashpour, P. Sharafi, B. Teodosio, A. Shringi, P. Mendis, Artificial intelligence and smart vision for building and construction 4.0: machine and deep learning methods and applications, Autom. Constr. 141 (2022) 104440, https://doi.org/10.1016/j.autcon.2022.104440.
[40] S. Kaewunruen, Q. Lian, Digital twin aided sustainability-based lifecycle management for railway turnout systems, J. Clean. Prod. 228 (2019) 1537–1551, https://doi.org/10.1016/j.jclepro.2019.04.156.
[41] S. Kaewunruen, N. Xu, Digital twin for sustainability evaluation of railway station buildings, Front. Built Environ. 4 (2018) 77, https://doi.org/10.3389/fbuil.2018.00077.
[42] G.P. Lydon, S. Caranovic, I. Hischier, A. Schlueter, Coupled simulation of thermally active building systems to support a digital twin, Energ. Build. 202 (2019) 109298, https://doi.org/10.1016/j.enbuild.2019.07.015.
[43] G. Angjeliu, D. Coronelli, G. Cardani, Development of the simulation model for digital twin applications in historical masonry buildings: the integration between numerical and experimental reality, Comput. Struct. 238 (2020) 106282, https://doi.org/10.1016/j.compstruc.2020.106282.
[44] S.M.E. Sepasgozar, Digital twin and web-based virtual gaming technologies for online education: a case of construction management and engineering, Appl. Sci. 10 (2020) 4678, https://doi.org/10.3390/app10134678.
[45] M. Antonino, M. Nicola, D.M. Claudio, B. Luciano, R.C. Fulvio, Office building occupancy monitoring through image recognition sensors, Int. J. Safe 9 (2019) 371–380, https://doi.org/10.2495/SAFE-V9-N4-371-380.
[46] Q. Lu, A.K. Parlikad, P. Woodall, G. Don Ranasinghe, X. Xie, Z. Liang, E. Konstantinou, J. Heaton, J. Schooling, Developing a digital twin at building and city levels: case study of West Cambridge Campus, J. Manag. Eng. 36 (2020) 05020004, https://doi.org/10.1061/(ASCE)ME.1943-5479.0000763.
[47] P.E.D. Love, J. Matthews, The 'how' of benefits management for digital technology: from engineering to asset management, Autom. Constr. 107 (2019) 102930, https://doi.org/10.1016/j.autcon.2019.102930.
[48] W. Jiang, L. Ding, C. Zhou, Digital twin: stability analysis for tower crane hoisting safety with a scale model, Autom. Constr. 138 (2022) 104257, https://doi.org/10.1016/j.autcon.2022.104257.
[49] Z. Zheng, W. Liao, J. Lin, Y. Zhou, C. Zhang, X. Lu, Digital twin-based investigation of a building collapse accident, Adv. Civil Eng. 2022 (2022) 1–13, https://doi.org/10.1155/2022/9568967.
[50] D. Lee, S. Lee, N. Masoud, M.S. Krishnan, V.C. Li, Digital twin-driven deep reinforcement learning for adaptive task allocation in robotic construction, Adv. Eng. Inform. 53 (2022) 101710, https://doi.org/10.1016/j.aei.2022.101710.
[51] C.-J. Liang, W. McGee, C.C. Menassa, V.R. Kamat, Real-time state synchronization between physical construction robots and process-level digital twins, Constr. Robot. 6 (2022) 57–73, https://doi.org/10.1007/s41693-022-00068-1.
[52] J. Canny, A computational approach to edge detection, IEEE Trans. Pattern Anal. Mach. Intell. PAMI-8 (1986) 679–698, https://doi.org/10.1109/TPAMI.1986.4767851.
[53] S. Biçici, M. Zeybek, An approach for the automated extraction of road surface distress from a UAV-derived point cloud, Autom. Constr. 122 (2021) 103475, https://doi.org/10.1016/j.autcon.2020.103475.
[54] J. Sun, B. Peng, C.C. Wang, K. Chen, B. Zhong, J. Wu, Building displacement measurement and analysis based on UAV images, Autom. Constr. 140 (2022) 104367, https://doi.org/10.1016/j.autcon.2022.104367.
[55] P. Kim, J. Park, Y.K. Cho, J. Kang, UAV-assisted autonomous mobile robot navigation for as-is 3D data collection and registration in cluttered environments, Autom. Constr. 106 (2019) 102918, https://doi.org/10.1016/j.autcon.2019.102918.
[56] S. Jia, C. Liu, X. Guan, H. Wu, D. Zeng, J. Guo, Bidirectional interaction between BIM and construction processes using a multisource geospatial data enabled point cloud model, Autom. Constr. 134 (2022) 104096, https://doi.org/10.1016/j.autcon.2021.104096.
[57] M. Kamari, Y. Ham, Vision-based volumetric measurements via deep learning-based point cloud segmentation for material management in jobsites, Autom. Constr. 121 (2021) 103430, https://doi.org/10.1016/j.autcon.2020.103430.
[58] M. Kamari, Y. Ham, AI-based risk assessment for construction site disaster preparedness through deep learning-based digital twinning, Autom. Constr. 134 (2022) 104091, https://doi.org/10.1016/j.autcon.2021.104091.
[59] Y. Ham, K.K. Han, J.J. Lin, M. Golparvar-Fard, Visual monitoring of civil infrastructure systems via camera-equipped unmanned aerial vehicles (UAVs): a review of related works, Vis. Eng. 4 (2016) 1, https://doi.org/10.1186/s40327-015-0029-z.
[60] E.P. Karan, R. Sivakumar, J. Irizarry, S. Guhathakurta, Digital modeling of construction site terrain using remotely sensed data and geographic information systems analyses, J. Constr. Eng. Manag. 140 (2014) 04013067, https://doi.org/10.1061/(ASCE)CO.1943-7862.0000822.
[61] T.-C. Huynh, Vision-based autonomous bolt-looseness detection method for splice connections: design, lab-scale evaluation, and field application, Autom. Constr. 124 (2021) 103591, https://doi.org/10.1016/j.autcon.2021.103591.
[62] F. Tang, C. Han, T. Ma, T. Chen, Y. Jia, Quantitative analysis and visual presentation of segregation in asphalt mixture based on image processing and BIM, Autom. Constr. 121 (2021) 103461, https://doi.org/10.1016/j.autcon.2020.103461.
[63] K. Mostafa, T. Hegazy, Review of image-based analysis and applications in construction, Autom. Constr. 122 (2021) 103516, https://doi.org/10.1016/j.autcon.2020.103516.
[64] I. Reda, A. Andreas, Solar position algorithm for solar radiation applications, Sol. Energy 76 (2004) 577–589, https://doi.org/10.1016/j.solener.2003.12.003.
[65] J.H. Meeus, Astronomical Algorithms, Willmann-Bell. Incorporated, Richmond, Virginia, USA, 1998. ISBN: 978–1607261452.
[66] P. Richens, Image processing for urban scale environmental modelling, in: Proceeding 5th International IBPSA Conference: Building Simulation 97, 1997, pp. 163–171, https://doi.org/10.26868/25222708.1997.95.
[67] Z.-H. Jiao, H. Ren, X. Mu, J. Zhao, T. Wang, J. Dong, Evaluation of Four Sky View Factor Algorithms Using Digital Surface and Elevation Model Data, Earth and Space Science 6, 2019, pp. 222–237, https://doi.org/10.1029/2018EA000475.
[68] I.D. Watson, G.T. Johnson, Graphical estimation of sky view-factors in urban environments, J. Climatol. 7 (1987) 193–197, https://doi.org/10.1002/joc.3370070210.
[69] F. Lindberg, C.S.B. Grimmond, The influence of vegetation and building morphology on shadow patterns and mean radiant temperatures in urban areas: model development and evaluation, Theor. Appl. Climatol. 105 (2011) 311–323, https://doi.org/10.1007/s00704-010-0382-8.
[70] N. Wallenberg, B. Holmer, F. Lindberg, D. Rayner, An anisotropic parameterization scheme for longwave irradiance and its impact on radiant load in urban outdoor settings, Int. J. Biometeorol. 67 (2023) 633–647, https://doi.org/10.1007/s00484-023-02441-3.
[71] M. Bruse, H. Fleer, Simulating surface–plant–air interactions inside urban environments with a three dimensional numerical model, Environ. Model Softw. 13 (1998) 373–384, https://doi.org/10.1016/S1364-8152(98)00042-5.
[72] A. Matzarakis, F. Rutz, H. Mayer, Modelling radiation fluxes in simple and complex environments—application of the RayMan model, Int. J. Biometeorol. 51 (2007) 323–334, https://doi.org/10.1007/s00484-006-0061-8.
[73] F. Lindberg, B. Holmer, S. Thorsson, SOLWEIG 1.0 – modelling spatial variations of 3D radiant fluxes and mean radiant temperature in complex urban settings, Int. J. Biometeorol. 52 (2008) 697–713, https://doi.org/10.1007/s00484-008-0162-7.
[74] S. Tsoka, A. Tsikaloudaki, T. Theodosiou, Analyzing the ENVI-met microclimate model's performance and assessing cool materials and urban vegetation applications–a review, Sustain. Cities Soc. 43 (2018) 55–76, https://doi.org/10.1016/j.scs.2018.08.009.
[75] J. Mao, L.K. Norford, Urban weather generator: Physics-based microclimate simulation for performance-oriented urban planning, in: M. Palme, A. Salvati (Eds.), Urban Microclimate Modelling for Comfort and Energy Studies, Springer International Publishing, Cham, 2021, pp. 241–263, https://doi.org/10.1007/978-3-030-65421-4_12.
[76] S. Deng, J. Ma, L. Zhang, Z. Jia, L. Ma, Microclimate simulation and model optimization of the effect of roadway green space on atmospheric particulate matter, Environ. Pollut. 246 (2019) 932–944, https://doi.org/10.1016/j.envpol.2018.12.026.
[77] B. Vinayak, H.S. Lee, S. Gedam, R. Latha, Impacts of future urbanization on urban microclimate and thermal comfort over the Mumbai metropolitan region, India, Sustain. Cities Soc. 79 (2022) 103703, https://doi.org/10.1016/j.scs.2022.103703.
[78] G. Evola, V. Costanzo, C. Magrì, G. Margani, L. Marletta, E. Naboni, A novel comprehensive workflow for modelling outdoor thermal comfort and energy demand in urban canyons: results and critical issues, Energ. Build. 216 (2020) 109946, https://doi.org/10.1016/j.enbuild.2020.109946.
[79] L. Chen, E. Ng, Outdoor thermal comfort and outdoor activities: a review of research in the past decade, Cities 29 (2012) 118–125, https://doi.org/10.1016/j.cities.2011.08.006.
[80] L. Tronchin, K. Fabbri, Energy and microclimate simulation in a heritage building: further studies on the Malatestiana library, Energies 10 (2017) 1621, https://doi.org/10.3390/en10101621.
[81] J. Graham, U. Berardi, G. Turnbull, R. McKaye, Microclimate analysis as a design driver of architecture, Climate 8 (2020) 72, https://doi.org/10.3390/cli8060072.
[82] N. Kántor, J. Unger, The most problematic variable in the course of human-biometeorological comfort assessment — the mean radiant temperature, Open Geosci. 3 (2011) 90–100, https://doi.org/10.2478/s13533-011-0010-x.

[83] S. Thorsson, J. Rocklöv, J. Konarska, F. Lindberg, B. Holmer, B. Dousset, D. Rayner, Mean radiant temperature – a predictor of heat related mortality, Urban Clim. 10 (2014) 332–345, https://doi.org/10.1016/j.uclim.2014.01.004.
[84] S. Manavvi, E. Rajasekar, Estimating outdoor mean radiant temperature in a humid subtropical climate, Build. Environ. 171 (2020) 106658, https://doi.org/10.1016/j.buildenv.2020.106658.
[85] P.O. Fanger, Thermal Comfort. Analysis and Applications in Environmental Engineering, Danish Technical Press, Copenhagen, 1970 (ISBN: 978-8757103410).
[86] P. Höppe, A new procedure to determine the mean radiant temperature outdoors, Wetter Leb 44 (1992) 147–151.
[87] F. Lindberg, S. Onomura, C.S.B. Grimmond, Influence of ground surface characteristics on the mean radiant temperature in urban areas, Int. J. Biometeorol. 60 (2016) 1439–1452, https://doi.org/10.1007/s00484-016-1135-x.
[88] O. Bäcklin, F. Lindberg, S. Thorsson, D. Rayner, N. Wallenberg, Outdoor heat stress at preschools during an extreme summer in Gothenburg, Sweden - preschool teachers' experiences contextualized by radiation modelling, Sustain. Cities Soc. 75 (2021) 103324, https://doi.org/10.1016/j.scs.2021.103324.
[89] N. Wallenberg, F. Lindberg, B. Holmer, S. Thorsson, The influence of anisotropic diffuse shortwave radiation on mean radiant temperature in outdoor urban environments, Urban Clim. 31 (2020) 100589, https://doi.org/10.1016/j.uclim.2020.100589.
[90] J. Konarska, F. Lindberg, A. Larsson, S. Thorsson, B. Holmer, Transmissivity of solar radiation through crowns of single urban trees—application for outdoor thermal comfort modelling, Theor. Appl. Climatol. 117 (2014) 363–376, https://doi.org/10.1007/s00704-013-1000-3.
[91] J. Hua, X. Zhang, C. Ren, Y. Shi, T.-C. Lee, Spatiotemporal assessment of extreme heat risk for high-density cities: a case study of Hong Kong from 2006 to 2016, Sustain. Cities Soc. 64 (2021) 102507, https://doi.org/10.1016/j.scs.2020.102507.
[92] P. Bröde, D. Fiala, K. Błażejczyk, I. Holmér, G. Jendritzky, B. Kampmann, B. Tinz, G. Havenith, Deriving the operational procedure for the universal thermal climate index (UTCI), Int. J. Biometeorol. 56 (2012) 481–494, https://doi.org/10.1007/s00484-011-0454-1.
[93] R. Stull, Wet-bulb temperature from relative humidity and air temperature, J. Appl. Meteorol. Climatol. 50 (2011) 2267–2269, https://doi.org/10.1175/JAMC-D-11-0143.1.
[94] ISO 7726, Ergonomics of the Thermal Environment-Instruments for Measuring Physical Quantities, 2nd ed, International Organization for Standardization, Switzerland, 1998, https://doi.org/10.31030/3123890. Case postale 56 CH-1211 Geneva 20.
[95] Occupational Safety and Health Administration (OSHA), OSHA Technical Manual, Section III: Chapter 4 Heat Stress. https://www.osha.gov/otm/section-3-health-hazards/chapter-4#wbgt, 2024 (accessed May 18, 2023).
[96] D. Fiala, G. Havenith, P. Bröde, B. Kampmann, G. Jendritzky, UTCI-Fiala multi-node model of human heat transfer and temperature regulation, Int. J. Biometeorol. 56 (2012) 429–441, https://doi.org/10.1007/s00484-011-0424-7.
[97] S. Park, S.E. Tuller, M. Jo, Application of universal thermal climate index (UTCI) for microclimatic analysis in urban thermal environments, Landsc. Urban Plan. 125 (2014) 146–155, https://doi.org/10.1016/j.landurbplan.2014.02.014.
[98] C. Di Napoli, F. Pappenberger, H.L. Cloke, Assessing heat-related health risk in Europe via the universal thermal climate index (UTCI), Int. J. Biometeorol. 62 (2018) 1155–1165, https://doi.org/10.1007/s00484-018-1518-2.
[99] A. Katal, S. Leroyer, J. Zou, O. Nikiema, M. Albettar, S. Belair, L. Leon Wang, Outdoor heat stress assessment using an integrated multi-scale numerical weather prediction system: a case study of a heatwave in Montreal, Sci. Total Environ. 865 (2023) 161276, https://doi.org/10.1016/j.scitotenv.2022.161276.
[100] C. Vitolo, C. Di Napoli, F. Di Giuseppe, H.L. Cloke, F. Pappenberger, Mapping combined wildfire and heat stress hazards to improve evidence-based decision making, Environ. Int. 127 (2019) 21–34, https://doi.org/10.1016/j.envint.2019.03.008.
[101] C. Roelofs, Without warning: worker deaths from heat 2014–2016, New Solut. 28 (2018) 344–357, https://doi.org/10.1177/1048291118777874.
[102] W. Köppen, Versuch einer Klassifikation der Klimate, vorzugsweise nach ihren Beziehungen zur Pflanzenwelt, Geogr. Z. 6 (1900) 657–679.
[103] N. Kántor, T.-P. Lin, A. Matzarakis, Daytime relapse of the mean radiant temperature based on the six-directional method under unobstructed solar radiation, Int. J. Biometeorol. 58 (2014) 1615–1625, https://doi.org/10.1007/s00484-013-0765-5.
[104] N.A. Kenny, J.S. Warland, R.D. Brown, T.G. Gillespie, Estimating the radiation absorbed by a human, Int. J. Biometeorol. 52 (2008) 491–503, https://doi.org/10.1007/s00484-008-0145-8.
[105] Z. Fang, T. Tang, Z. Zheng, X. Zhou, W. Liu, Y. Zhang, Thermal responses of workers during summer: an outdoor investigation of construction sites in South China, Sustain. Cities Soc. 66 (2021) 102705, https://doi.org/10.1016/j.scs.2020.102705.
[106] F.R. d'Ambrosio Alfano, M. Dell'Isola, B.I. Palella, G. Riccio, A. Russi, On the measurement of the mean radiant temperature and its influence on the indoor thermal environment assessment, Build. Environ. 63 (2013) 79–88, https://doi.org/10.1016/j.buildenv.2013.01.026.
[107] W. Ouyang, Z. Liu, K. Lau, Y. Shi, E. Ng, Comparing different recalibrated methods for estimating mean radiant temperature in outdoor environment, Build. Environ. 216 (2022) 109004, https://doi.org/10.1016/j.buildenv.2022.109004.
[108] E. Teitelbaum, K.W. Chen, F. Meggers, H. Guo, N. Houchois, J. Pantelic, A. Rysanek, Globe thermometer free convection error potentials, Sci. Rep. 10 (2020) 2652, https://doi.org/10.1038/s41598-020-59441-1.
[109] J.K. Vanos, K. Rykaczewski, A. Middel, D.J. Vecellio, R.D. Brown, T.J. Gillespie, Improved methods for estimating mean radiant temperature in hot and sunny outdoor settings, Int. J. Biometeorol. 65 (2021) 967–983, https://doi.org/10.1007/s00484-021-02131-y.
[110] J.A. Acero, A. Dissegna, Y.S. Tan, A. Tan, L.K. Norford, Outdoor performance of the black globe temperature sensor on a hot and humid tropical region, Environ. Technol. 44 (2023) 961–973, https://doi.org/10.1080/09593330.2021.1989057.
[111] C.V. Gál, N. Kántor, Modeling mean radiant temperature in outdoor spaces, A comparative numerical simulation and validation study, Urban Clim. 32 (2020) 100571, https://doi.org/10.1016/j.uclim.2019.100571.
[112] Y.-C. Chen, T.-P. Lin, A. Matzarakis, Comparison of mean radiant temperature from field experiment and modelling: a case study in Freiburg, Germany, Theor. Appl. Climatol. 118 (2014) 535–551, https://doi.org/10.1007/s00704-013-1081-z.
[113] C.T. Pereira, É. Masiero, V. Bourscheidt, Socio-spatial inequality and its relationship to thermal (dis)comfort in two major local climate zones in a tropical coastal city, Int. J. Biometeorol. 65 (2021) 1177–1187, https://doi.org/10.1007/s00484-021-02099-9.
[114] National Oceanic and Atmospheric Administration (NOAA), Heat Index Chart. https://www.weather.gov/ffc/hichart, 2024 (accessed July 31, 2023).
[115] K. Błażejczyk, G. Jendritzky, P. Bröde, D. Fiala, G. Havenith, Y. Epstein, A. Psikuta, B. Kampmann, An introduction to the universal thermal climate index (UTCI), Geogr. Pol. 86 (2013) 5–10, https://doi.org/10.7163/GPol.2013.1.
[116] C. Vancutsem, P. Ceccato, T. Dinku, S.J. Connor, Evaluation of MODIS land surface temperature data to estimate air temperature in different ecosystems over Africa, Remote Sens. Environ. 114 (2010) 449–465, https://doi.org/10.1016/j.rse.2009.10.002.
[117] A. Hsu, G. Sheriff, T. Chakraborty, D. Manya, Disproportionate exposure to urban heat island intensity across major US cities, Nat. Commun. 12 (2021) 2721, https://doi.org/10.1038/s41467-021-22799-5.
[118] J. Cao, W. Zhou, Z. Zheng, T. Ren, W. Wang, Within-city spatial and temporal heterogeneity of air temperature and its relationship with land surface temperature, Landsc. Urban Plan. 206 (2021) 103979, https://doi.org/10.1016/j.landurbplan.2020.103979.
[119] N.C. Pepin, E.E. Maeda, R. Williams, Use of remotely sensed land surface temperature as a proxy for air temperatures at high elevations: findings from a 5000 m elevational transect across Kilimanjaro, J. Geophys. Res. Atmos. 121 (2016) 9998, https://doi.org/10.1002/2016JD025497.
[120] T. Omar, M.L. Nehdi, Remote sensing of concrete bridge decks using unmanned aerial vehicle infrared thermography, Autom. Constr. 83 (2017) 360–371, https://doi.org/10.1016/j.autcon.2017.06.024.
[121] N.N. Kulkarni, K. Raisi, N.A. Valente, J. Benoit, T. Yu, A. Sabato, Deep learning augmented infrared thermography for unmanned aerial vehicles structural health monitoring of roadways, Autom. Constr. 148 (2023) 104784, https://doi.org/10.1016/j.autcon.2023.104784.
[122] F. Liu, J. Liu, L. Wang, Deep learning and infrared thermography for asphalt pavement crack severity classification, Autom. Constr. 140 (2022) 104383, https://doi.org/10.1016/j.autcon.2022.104383.
[123] M.V. Rodríguez, S.G. Melgar, J.M.A. Márquez, Assessment of aerial thermography as a method of in situ measurement of radiant heat transfer in urban public spaces, Sustain. Cities Soc. 87 (2022) 104228, https://doi.org/10.1016/j.scs.2022.104228.
[124] O. Golovina, J. Teizer, N. Pradhananga, Heat map generation for predictive safety planning: preventing struck-by and near miss interactions between workers-on-foot and construction equipment, Autom. Constr. 71 (2016) 99–115, https://doi.org/10.1016/j.autcon.2016.03.008.
[125] C. Dong, F. Wang, H. Li, L. Ding, H. Luo, Knowledge dynamics-integrated map as a blueprint for system development: applications to safety risk management in Wuhan metro project, Autom. Constr. 93 (2018) 112–122, https://doi.org/10.1016/j.autcon.2018.05.014.
[126] T. Maruyama, S. Kanai, H. Date, Tripping risk evaluation system based on human behavior simulation in laser-scanned 3D as-is environments, Autom. Constr. 85 (2018) 193–208, https://doi.org/10.1016/j.autcon.2017.10.011.
[127] X. Li, G. Wang, Examining runner's outdoor heat exposure using urban microclimate modeling and GPS trajectory mining, Comput. Environ. Urban. Syst. 89 (2021) 101678, https://doi.org/10.1016/j.compenvurbsys.2021.101678.
[128] H. Cai, X. Li, Z. Chen, L. Kong, Fast identification of multiple indoor constant contaminant sources by ideal sensors: a theoretical model and numerical validation, Indoor Built Environ. 22 (2013) 897–909, https://doi.org/10.1177/1420326X12463584.
[129] G. Fobiri, I. Musonda, F. Muleya, Reality capture in construction project management: a review of opportunities and challenges, Buildings 12 (2022) 1381, https://doi.org/10.3390/buildings12091381.
[130] A. Ibrahim, M. Golparvar-Fard, K. El-Rayes, Metrics and methods for evaluating model-driven reality capture plans, Comp. Aid. Civil Eng 37 (2022) 55–72, https://doi.org/10.1111/mice.12693.